International Journal of Nanomedicine

Dovepress
Taylor & Francis Group

Open Access Full Text Article

ORIGINAL RESEARCH

Cellular Synthesis of Targeted Ultrasound Molecular Imaging Probe and Its Application in Prostate Cancer Diagnosis

Zhenzhou Li[1,*], Tingting Liu[1,*], Tao Cui[2,*], Xiong Shen[1,3], Chenxing Liu[4], Fei Yan[4]

[1]Department of Ultrasound, The Second People's Hospital of Shenzhen, The First Affiliated Hospital of Shenzhen University, Shenzhen, 518061, People's Republic of China; [2]Nuclear Medicine Department, Shenzhen Hezheng Hospital, Shenzhen, 518055, People's Republic of China; [3]Graduate School, Guangxi University of Chinese Medicine, Nanning, 530200, People's Republic of China; [4]State Key Laboratory of Quantitative Engineering Biology, Shenzhen Institute of Synthetic Biology, Shenzhen Institutes of Advanced Technology, Chinese Academy of Sciences, Shenzhen, 518055, People's Republic of China

*These authors contributed equally to this work

Correspondence: Fei Yan, Email fei.yan@siat.ac.cn

International Journal of Nanomedicine downloaded from https://www.dovepress.com/
For personal use only.

Purpose: The traditional construction of targeted ultrasound molecular imaging probes relies on multistep chemical synthesis strategies, which are time-consuming and inefficient, thereby limiting technological advancements. To address this, we developed a novel genetic engineering approach for biosynthesizing targeted nanoprobes for prostate cancer diagnosis.

Materials and Methods: The anti-PSMA nanobody-encoding gene was fused to the C-terminus of the gas vesicle structural protein gene GvpC and cloned into a pBV220 plasmid with a hyperthermia-responsive gene expression circuit. This recombinant plasmid was transformed into *E. coli* BL21(A1) harboring pET-28a-ΔGvpC-eGVs plasmids to create PSMA-GVs@*E. coli* genetically engineered bacteria. The probe assembly were involved in two-step gene expression procedure. ΔGvpC-eGVs were first induced by IPTG, followed by temperature-triggered (42°C) production of PSMA-GvpC proteins that spontaneously assembled onto GVs.

Results: The biosynthesized PSMA-eGVs probes exhibited a uniform size (100–200 nm) and demonstrated excellent targeting capability in prostate cancer cells. In vivo studies confirmed effective tumor vascular penetration and specific binding with PSMA-positive tumor cells, resulting in significantly stronger acoustic signals than the non-targeted EGFP-eGVs controls.

Conclusion: This cellular synthesis strategy enables efficient production of targeted ultrasound molecular imaging probes through genetically engineering technology, providing a promising platform for precision cancer diagnostics.

Keywords: ultrasound molecular imaging, targeted ultrasound molecular imaging probe, prostate cancer diagnosis, gas vesicles, cellular synthesis

Introduction

Prostate cancer is the most commonly malignancy in men globally, predominantly in high human development index regions. Current clinical serum PSA testing lacks specificity, leading to over-diagnosis and unnecessary biopsies.[1] Conventional ultrasound imaging is difficult to differentiate between benign and malignant lesions and cannot visualize key biomarkers like prostate-specific membrane antigen (PSMA) in vivo.[2] In recent years, ultrasound molecular imaging technology based on targeted probes provides a promising approach to detect the expression PSMA at molecular level, making it possible early diagnosis of prostate cancer,[3,4] However, advancements in ultrasound molecular imaging have long been limited by the complex fabrication process of targeted probes.[5] Conventional chemical synthesis strategies rely on multistep coupling reactions, including ligand activation, purification, and covalent conjugation to microbubbles via NHS/EDC crosslinking, biotin-avidin systems, or maleimide-thiol reactions.[6–8] These methods have many obvious drawbacks, including complex and time-consuming procedures (typically 3–5 days), random ligand orientation, and

Received: 4 September 2025
Accepted: 12 December 2025
Published: 30 December 2025

© 2025 Li et al. This work is published and licensed by Dove Medical Press Limited. The full terms of this license are available at https://www.dovepress.com/terms.php and incorporate the Creative Commons Attribution – Non Commercial (unported, v4.0) License (http://creativecommons.org/licenses/by-nc/4.0/). By accessing the work you hereby accept the Terms. Non-commercial uses of the work are permitted without any further permission from Dove Medical Press Limited, provided the work is properly attributed. For permission for commercial use of this work, please see paragraphs 4.2 and 5 of our Terms (https://www.dovepress.com/terms.php).

batch-to-batch heterogeneity. Furthermore, chemical crosslinkers can induce immunogenic reactions, bring with safety concerns for clinical use.[9]

In recent years, gas vesicles (GVs), which are evolutionarily conserved buoyancy organelles initially discovered in *Cyanobacteria* and *Halophilic archaea*, offer a transformative solution.[10–12] Their unique physicochemical properties make them ideal ultrasound contrast agents. Spindle- or cylinder-shaped nanostructures (width: 45–250 nm; length: 100–600 nm) comprise a pure protein shell devoid of lipids or carbohydrates. The 2 nm thick shell features a hydrophobic inner wall that permitted gas exchange while excluding liquid water, thus forming a thermodynamically stable gas-filled cavity. Crucially, GVs undergo reversible collapse under specific hydrostatic pressures, generating nonlinear ultrasound signals essential for high-contrast imaging.[13–15] GV biogenesis is governed by 8–14 genes cluster (such as GvpA and GvpC), where the structural protein GvpA forms a ribbed skeleton, whereas the scaffolding protein GvpC enhances mechanical stability through repetitive N-terminal motifs anchored to the vesicle surface.[16–18] Notably, the C-terminal domain of GvpC can serves as a plastic fusion site for exogenous functional proteins,[19–21] providing a genetic engineering basis for designing target probes capable of specifically binding with biomarkers such as PSMA. However, single-plasmid co-expression strategies—directly fusing antibody genes to the GvpC C-terminus under a single promoter—face unresolved challenges. For example, steric hindrance between large antibody Fc domains and the GV-binding region of GvpC causes misfolding, while imbalanced expression disrupts the stoichiometry of GV assembly proteins. Additionally, competition between the N-terminal GV-binding and C-terminal antibody domains for post-translational modifications reduces the antigen-binding affinity.[20,22–24]

To overcome these issues, we engineered a dual-plasmid thermal induction gene expression system for the efficient biosynthesis of prostate-specific membrane antigen (PSMA)-targeted GVs probes. Firstly, a GvpC-deleted DNA fragment, amplified from the *Serratia sp. ATCC*39006 GV gene cluster, was cloned into the pET-28a vector using the Gibson assembly. This generated pET-28a-ΔGvpC-eGVs plasmid, enabling robust GV scaffold formation (Figure 1a). Next, a high-affinity PSMA nanobody gene was fused to the C-terminus of GvpC and cloned into the pBV220 plasmid under the pR/pL promoter, producing the targeting plasmid pBV220-PSMA-GvpC (Figure 1b). Co-transformation of both plasmids into *E. coli BL*21(A1) generated the engineered PSMA-GVs@*E. coli* strain. A two-step thermal induction program enabled controllable probe assembly: the ΔGvpC-eGVs scaffolds were firstly produced by IPTG (Isopropyl-beta -D-thiogalactopyranoside) induction at 30°C, followed by a thermal upshift to 42°C to trigger the expression of GvpC-PSMA. The specific interaction between the GvpC N-terminal repeat motif and GV protein shell driven GvpC-PSMA to anchor onto GVs and form targeted nanoprobes termed as PSMA-eGVs (Figure 1c). These probes will be utilized for precision ultrasound molecular imaging in prostate tumor-bearing mice, enabling the evaluation of their diagnostic efficacy and practical applicability (Figure 1d).

Materials and Methods

Materials

All restriction enzymes were from New England Biolabs (NEB) and the ligase was from Beyotime Biotechnology. LB medium (no sugar) (one liter contains 10 g tryptone, 5 g yeast extract, and 5 g NaCl) and LB agar (without sugar) (LB medium with agar 15 g/1 L) from HuanKai Microbial were used for *E. coli* strain cultivation. Anti-PSMA polyclonal antibody (Cat No. 13163-1-AP) was purchased from Proteintech Ltd. Fluorescein isothiocyanate N-Hydroxy succinimide Ester (FITC-NHS; CAS Number: R-FF-005-2-50mg; Brand: Ruixibio) was produced by Risi Bio. SoluLyse Bacterial Protein Extraction Reagent (Tris Buffer) was purchased from Shenzhen Chemical Test Technology Co., Ltd. (Item Number: L200500, Brand: Galantis, Shenzhen, China). Lysozyme (Item number: L8120-50g, Brand: Soleibao, Beijing, China) and DNase I (CAS Number: 9003-98-9, Brand: GLPBIO, Shang hai, China) were purchased from Beyotime Institute of Biotechnology. Fludeoxyglucose ^{18}F-prostaic membrane-specific antigen injection ^{18}F-PSMA was provided by the Medical Imaging Center of Shenzhen Yunshan Yunli Hospital. BALB/c nude mice (~20 g each) were obtained from the Guangdong Medical Experimental Animal Center.

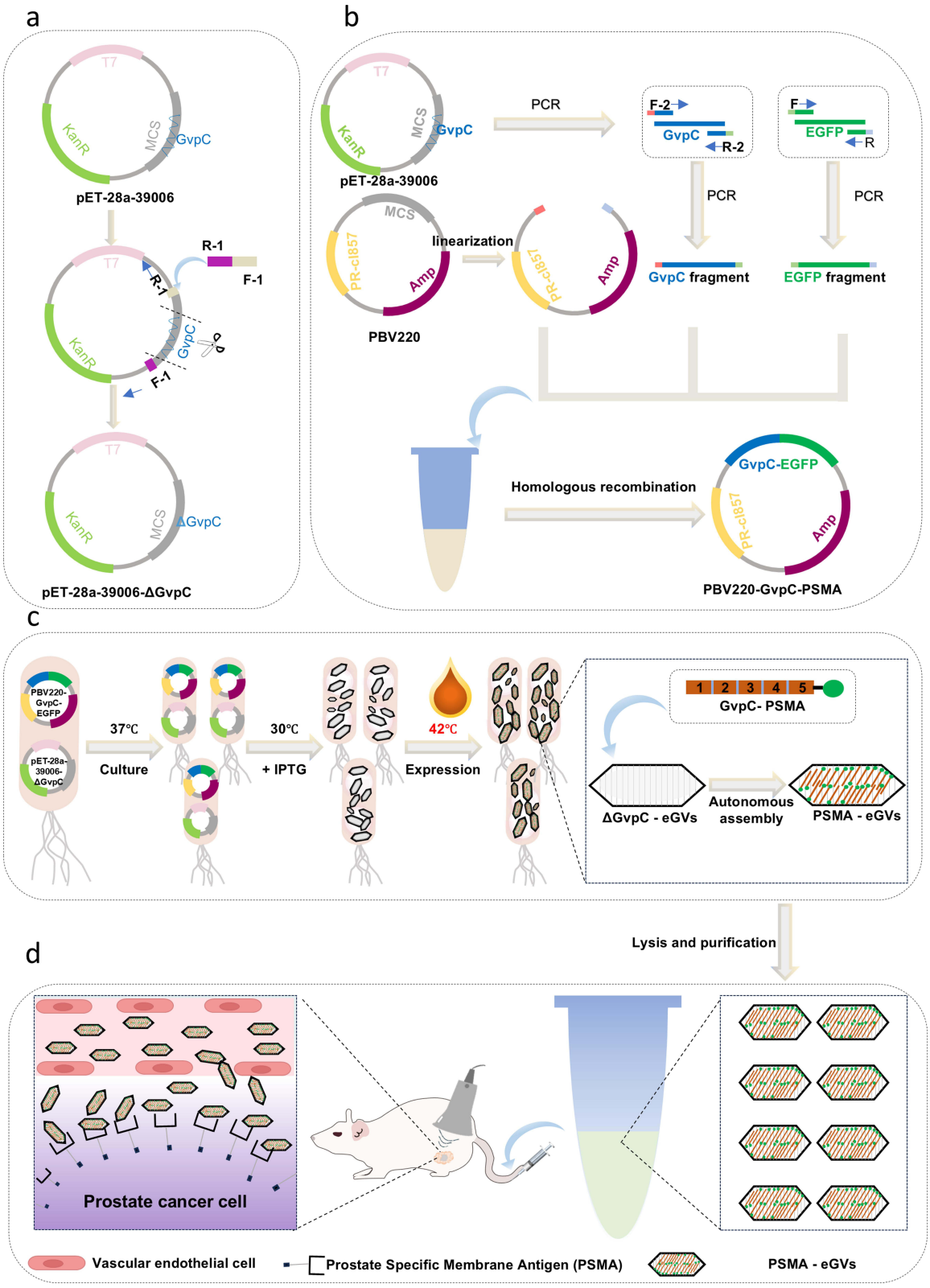

Figure 1 Schematic of the one-step genetic-engineering strategy for constructing PSMA-targeted ultrasound nanoprobes (PSMA-eGVs). (**a**) Construction of plasmid pET-28a-ΔGvpC-eGVs encoding the gas vesicle structural proteins. (**b**) Construction of inducible plasmid pBV220-GvpC-PSMA for fusion protein expression. (**c**) Co-transformation of both plasmids into *E. coli* BL21(A1) and two-step induction: IPTG (30°C) for GVs scaffold formation, followed by thermal upshift (42°C) to drive fusion protein expression and self-assembly of PSMA-eGVs. (**d**) Purification of nanoprobes and intravenous administration for targeted ultrasound molecular imaging of transplanted prostate tumors.

https://doi.org/10.2147/IJN.S561230

Cellular Synthesis of Targeted Ultrasound Molecular Imaging Probe

(1) Plasmids and Primers: The pET28a-39006 plasmid was constructed following previously described method.[25] Briefly, the GV-encoding gene cluster was cloned from Serratia 39006 and inserted into the pET28a (+) vector using Gibson assembly. Subsequently, the pET28a-39006-ΔGvpC plasmid was generated by knocking out GvpC gene using homologous recombination and PCR. The PBV220-GvpC-EGFP plasmid was constructed via a three-step procedure: 1) the parental PBV220-FAST-PET plasmid was linearized by EcoRI and BamHI (Thermo Fisher Scientific) digestion; 2) By using primers with homologous arms for amplification, GvpC and EGFP fragments were obtained. They were then directly cloned into the linearized vector PBV220 using the ClonExpress Ultra one-step cloning kit; 3) recombinant plasmids were transformed into *E. coli* DH5α competent cells (TransGen Biotech) and validated by colony PCR, restriction digestion, and Sanger sequencing. The PBV220-GvpC-PSMA plasmid was constructed through the following steps: firstly, the PBV220-GvpC-EGFP template (provided by Qingke Biotechnology Co., Ltd.) was linearized using reverse PCR technology to obtain PBV220-GvpC. Subsequently, it was combined with an anti-PSMA nanobody gene fragment that had been optimized for codons (designed based on patent CN202310850291.2) through homologous recombination. The detailed information regarding the bacterial strains, primers, and plasmids used in this study was provided in Tables S1–S3 of the Supplementary Materials.

(2) Synthesis of targeted GVs: GVs were synthesized by co-transforming pET28a-39006-ΔGvpC with either PBV220-GvpC-EGFP or PBV220-GvpC-PSMA into *E. coli* BL21(A1) competent cells using a standard heat-shock protocol (30 min on ice, 90 s at 42°C, 2 min on ice), followed by recovery in 1 mL antibiotic-free LB medium at 37°C and 200 rpm for 1 h. Transformants were selected on LB agar plates containing kanamycin (50 μg/mL) and ampicillin (100 μg/mL), and single colonies were inoculated into 5 mL LB medium supplemented with the same antibiotic and 1% glucose for overnight culture. For large-scale production, the culture was diluted 1:100 into 500 mL LB medium with antibiotics and 0.2% glucose, grown to OD_{600} = 0.6–0.8 at 37°C, and induced with 0.4 mM IPTG and 0.5% L-arabinose at 30°C for 22 h, followed by incubation at 42°C for ≥16 h to promote GV assembly. Subsequently, the harvested *E. coli* cells expressing EGFP-eGVs were applied to a confocal dish for observation. The gas vesicle production and concomitant EGFP fluorescence were then assessed using high-resolution confocal microscopy (A1R, Nikon, Japan,).

(3) Extraction and purification of targeted GVs: After allowing the mature bacterial cultures to stand for 2–3 days, bacteria containing GVs naturally floated to the top. Those bacteria that floated or floated slowly were transferred to a 50 mL centrifuge tube and subjected to low-speed centrifugation (600×g, 2 h, 4 °C). The supernatant obtained was mixed with bacterial lysis buffer (containing DNase I enzymes and lysozyme) and incubated overnight at room temperature to achieve complete cell lysis. Subsequently, three to five differential centrifugations (600×g, 3 h, 4 °C) were used to achieve further purification. The enriched GVs portion was isolated and stored at 4 °C for subsequent use. Subsequently, we analyzed wild-type gas vesicles (39006WT-GVs) and GvpC knockout mutants (39006ΔGvpC-eGVs) using SDS-PAGE (Presgained Color Protein Marker, Item number: BL706A, Tris-Glycine 4–20%) to validate their successful construction. To observe the morphology and distribution of the purified EGFP-eGVs particles, we conducted super-resolution fluorescence imaging using a structured illumination microscope (Nikon, N-SIM). In brief, the purified EGFP-eGVs samples were dropped onto the cover glass of the confocal microplate and imaging was performed with a 100× oil-immersion objective lens (NA 1.49), using 488 nm laser excitation and a 525/50 nm emission filter. Super-resolution images were acquired with 3 rotations and 5 phases per slice, and reconstructed using the NIS-Elements AR software to achieve approximately 120 nm lateral resolution.

(4) Proteomic analysis: 200μL of GVs was added to an equal volume of RIPA lysate (50 mM Tris pH 7.4, 150 mM NaCl, 1% Triton X-100, 1% sodium deoxycholate, 0.1% SDS) and sonicated (30% power, 3s on /5s off); After that, the supernatant was collected by centrifugation at 17,000×g for 15 min at 4 °C. After determination of protein concentration by BCA method, 100 μg of protein was digested by FASP: Denaturation with 8M urea, reduction alkylation with 10 mM Tris(2-carboxyethyl) phosphine (TCEP) and 40 mM Chloroacetamide (CAA) for 30 min, after washing with 50 mM Triethylammonium bicarbonate (TEAB) in a 10 kDa ultrafiltration tube, 0.5 μg trypsin was added for enzymatic digestion at 37°C for 16 h. The peptides were activated with Acetonitrile (ACN), washed by equilibration with water

formic acid, eluted with 40% and 50% ACN (containing 0.1% formic acid), and concentrated at 45 ° C. Finally, 200 ng peptide was used for 60 min gradient LC-MS/MS (Bruker timsTOF pro) (Data-Dependent Acquisition mode) analysis.

Characterization of PSMA-eGVs and EGFP-eGVs

EGFP-expressing *E. coli* cells and purified EGFP-eGVs were imaged using an inverted phase-contrast microscope (PCM, Olympus IX83, Tokyo, Japan). The samples were diluted in PBS to an optimal density, placed on a glass slide pre-coated with a 1% agarose pad, and covered with a coverslip. Phase-contrast images were acquired at room temperature using a ×100 oil-immersion objective. GV concentration was determined at a wavelength of 500 nm using a microplate reader (Multiscan GO; Thermo Scientific, Waltham, MA, United States). The GVs were observed using transmission electron microscopy (TEM; Hitachi H-7500, Hitachi Limited, Tokyo, Japan). The samples were diluted, carefully placed on a copper mesh, negatively stained with 2% phosphotungstic acid, and dried at room temperature. TEM was used to observe the morphology of GVs. The size, zeta potential, and polydispersity index of PSMA-eGVs and EGFP-eGVs were characterized using a dynamic light scattering detector (Zetasizer Nano ZS; Malvern, Westborough, Mass, USA) at 25 °C. The obtained targeting probe PSMA-eGVs were placed at 4 °C for different times, and their particle size and surface potential were measured to evaluate the stability of the targeting probe.

In vitro Ultrasound Imaging

An in vitro imaging phantom was prepared using a custom-made 2% (w/v) agarose mold. Subsequently, different concentrations of PSMA-eGVs and EGFP-eGVs (OD_{500} = 1.0, 1.5, 2.0, 2.5, 3.0, and 3.5) were added to the wells. Imaging was performed using an ultrasound diagnostic device (Mindray Resona 9T; Mindray, Shenzhen, China) equipped with an L11-3U linear-array transducer. The ultrasonic probe was then placed directly on the agarose. The parameters were as follows: acoustic power: 15.49%, mechanical index: 0.320, contrast gain: 70 dB.

Cell Culture

Both PC-3 cells and LNCap-3 cells were purchased from the American Type Culture Collection. PC-3 cells were cultured in Ham's F-12K (Item Number:PM150910) medium containing 10% fetal calf serum (Gibco), and 1% penicillin −streptomycin solution, and kept in a humidified atmosphere containing 5% CO_2 at 37°C. LNCap-3 cells were cultured in RPMI-1640 (Item Number: G4535) medium containing 20% fetal calf serum (Gibco), and 1% penicillin−streptomycin solution, and kept in a humidified atmosphere containing 5% CO_2 at 37°C. When these cultured cells reached about 80% confluence in the Corning's Cell Bind cell culture flasks (Product item number: 3289), they were passaged or stored for future use.

In vitro Cell Targeting Studies

To assess cell targeting, 80% confluent LNCap and PC-3 cells were harvested, resuspended in 500 μL PBS in 1.5 mL microcentrifuge tubes, and fixed with 4% paraformaldehyde. Next, 10 μL (OD_{500} 1.5) of FITC-labeled PSMA-eGVs according to the method described in the previous article.[26] Briefly, PSMA-eGVs were conjugated to FITC-NHS ester in a tube with gentle rotation in the dark at 4°C. The resulting solution was then dialyzed against PBS (pH 7.4) at 4°C using cellulose membranes (MWCO 3 kDa; Solarbio) to remove any unreacted dye. For competitive binding assays, the cell surface PSMA receptor was blocked with free anti-PSMA polyclonal antibody and incubated with 10 μL FITC-PSMA-eGVs for 30 min. The cells were then analyzed by a flow cytometry analyzer equipped with a 488 nm laser (Model: CytoFLEX S). The detection was carried out using the FITC channel, with a 525/40 nm band-pass filter. Data analysis employed a sequential gating strategy. All data were analyzed using the FlowJo software (version 10.8.1). For cell adhesion studies, LNCap and PC-3 cells were seeded in 24-well plates and allowed to adhere overnight and fixed with 4% paraformaldehyde. 100 μL FITC-PSMA-eGVs or EGFP-eGVs (OD_{500} 1.5) were added to each well and the plate was incubated at room temperature in the dark for 10 min. After washing three times (5 min each) with cold PBS, the nuclei were counterstained with DAPI, and cell binding was observed using a confocal microscope (A1R, Nikon, Japan). Competitive inhibition was assessed by incubation with free anti-PSMA polyclonal antibody for 30 min at room temperature prior to the addition of FITC-PSMA-eGVs.

Animal Model

All animal experiments were performed in compliance with relevant laws and institutional guidelines for the care and use of laboratory animals. The protocols were approved by the Committee on the Ethics of Animal Experiments of the Shenzhen Institutes of Advanced Technology, Chinese Academy of Science (protocol NO: SIAT-IACUC-231114-HCS-YF-A2377; date of approval: November 14, 2023). All imaging procedures were performed under isoflurane inhalation anesthesia, and efforts were made to minimize suffering. Briefly, BALB/c nude mice. (≈20 g each) mice (n = 20) were obtained from the Medical Experimental Animal Center. The xenograft tumor model was established by subcutaneous injection of 2×10^7 PC-3 or LNCap cells into the right hind limb. Small tumors (n = 10) were defined as tumors with a diameter of < 8 mm, and large tumors (n = 10) were defined as tumors with a diameter of > 10 mm. Mice bearing small or large tumors were used for UMI, PET/CT experiments and histological analysis.

In vivo Ultrasound Imaging

In the experimental operation, the mice were first anesthetized and fixed. The mice were placed in an induction box and anesthetized with isoflurane gas. The concentration was set at 4–5% during the induction stage and adjusted to 0.5–1.5% to maintain the anesthetic state, ensuring a moderate level of anesthesia. Then, hair removal cream was applied to remove the hair around the tumor and the area surrounding it. The area was wiped with a paper towel moistened with physiological saline to remove any remaining hair and hair removal cream. Subsequently, the mice were placed in a right lateral position on the experimental table and a layer of ultrasound coupling agent was evenly applied to the imaging area. The probe was fixed in position relative to the tumor. Mice bearing LNCap or PC-3 tumors were randomly administered with PSMA-eGVs or EGFP-eGVs (200 μL, OD_{500} = 3.5) via tail vein injection by using of a 1 mL syringe. The contrast images of tumor were then acquired using the same parameters described above and monitored continuously for 10 minutes. After acquisition, a short high-power pulse was applied to collapse the GVs in the tumor to avoid interference with other probes. The perfusion region at the time of peak perfusion was defined as the region of interest (ROI). Images were processed and quantified using ImageJ software. The mean gray signal value at each time point was used to obtain the time-intensity curve (TIC).

In vivo PET-CT Imaging

Mice bearing small or large LNCap or PC-3 tumors were intravenously injected with ^{18}F-PSMA (Manufacturer: Andiko) (2.8 MBq per mouse) via the tail vein. At 90 minutes post-injection, each mouse was anesthetized by intraperitoneal administration of 1 mg Zoletil 50. Static PET-CT scans were then performed under anesthesia using a United Imaging uMI 780 PET/CT system. The acquired data were reconstructed using the OSEM algorithm. Regions of interest (ROIs) for the tumors were delineated using PMOD software, and the maximum standardized uptake value (SUVmax) was calculated.

Histological Examination

Mice bearing small and large tumors were euthanized (A controlled flow rate of 20–30% chamber volume per minute of carbon dioxide was used for euthanasia)., and tumor tissues were dissected for immunohistochemical detection. Tumor sections 6 μm thick were cut using a freezing microtome (CM 1950, Leica, Heidelberg, Germany) and stained with anti-PSMA monoclonal antibody (GB115710). Tissue fluorescence was observed using an inverted fluorescence microscope (Wuhan Saiwei Bio-Technology Co., Ltd., China).

Biosafety Testing

For the hemolysis assay, 1 mL of fresh blood was collected from BALB/c nude mice and diluted with 2 mL PBS. Red blood cells (RBCs) were isolated from serum by centrifugation (3000 RCF for 5 min). After washing five times, RBCs were diluted with 10 mL of PBS. The RBC suspension (250 μL) was incubated with 1 mL of PBS (negative control), distilled water (positive control), and PSMA-eGVs at different concentrations (OD_{500} at 1.0, 1.5, 2.0, 2.5, 3.0, 3.5) for 3 h at 37°C. After that, the supernatant was centrifuged at 600 × g for 2 h, the absorbance of the supernatant (200 μL) at

541 nm was measured using a microplate reader (Multiscan GO, Thermo Scientific, Waltham, MA, United States), and the hemolysis rate was calculated.

For in vivo biosafety, 12 healthy mice were systemically injected with PBS, PSMA-eGVs, or EGFP-eGVs (200 μL, OD_{500} = 3.5). Blood samples were collected from the ophthalmic artery after seven days to detect liver function (alanine aminotransferase (ALT) and aspartate aminotransferase (AST)) and renal function (blood urea nitrogen (BUN) and creatinine (CREA)). Subsequently, the major organs (heart, liver, spleen, lungs, and kidneys) were removed and fixed with paraformaldehyde (4%, w/v) for HE staining (Wuhan Servicebio Technology Company, China).

Statistical Analysis

Data are expressed as the mean ± standard deviation, and an independent *t*-test was used to compare the two groups. Multiple group comparisons were performed using one-way ANOVA followed by Bonferroni's multiple comparison test. We used simple linear regression analysis to correlate UMI signals with PET signals. Briefly, the maximum standardized uptake value of PET was set as the independent variable (X), and the area under the curve of the ultrasound molecular imaging signal was set as the dependent variable (Y). All analyses were completed using GraphPad Prism 9.5.1 (733) software. All analyses were completed using GraphPad Prism 9.5.1 (733) software. *P < 0.05, considered significant. **** for P < 0.0001.

Results

Cultivation and Purification of EGFP-eGVs and PSMA-eGVs

Successful construction of the recombinant plasmids was verified by PCR screening of bacterial colonies (Figures S1 and S2). The two plasmids (pET-28a-39006ΔGvpC and either pBV220-GvpC-PSMA or pBV220-GvpC-EGFP) were cotransformed into *E. coli* BL21(A1). Transformants were cultured and subjected to a two-step induction process to express and assemble the targeted GVs. Using EGFP as the reporter gene, we validated the feasibility of the dual-plasmid expression system. Confocal microscopy analysis of the engineered bacterial strains revealed characteristic white gas vesicle structures under bright-field illumination, accompanied by intense EGFP fluorescence signals in the corresponding channel. The spatial co-localization of these signals in the merged images demonstrated gas vesicle formation and reporter gene expression (Figure 2a, top row). Furthermore, nanoscale fluorescence microscopy of purified EGFP-eGVs corroborated these findings (Figure 2a, bottom row), providing additional evidence for the robustness of the genetic circuit. Collectively, these results confirm the functionality of the engineered system in concurrently generating gas vesicles and expressing heterologous proteins. Subsequently, the EGFP fragment was replaced with a PSMA-targeting nanobody fragment to construct a dual-plasmid system (Figures S3 and S4). To verify the accuracy of the constructs, wild-type gas vesicles (39006WT-GVs) and the GvpC knockout mutant (39006ΔGvpC-eGVs) as the control were analyzed by SDS-PAGE. SDS-PAGE results indicated the absence of the ~18-kDa GvpC band in the 39006ΔGvpC-eGVs sample (Figure 2b, blue dashed box). Proteomic analysis via LC-MS/MS confirmed the complete absence of GvpC peptides in 39006ΔGvpC-eGVs, whereas GvpC content in EGFP-eGVs was comparable to that in 39006WT-GVs (Figure 2c). Consistently, the protein profile of PSMA-eGVs was identical to that of EGFP-eGVs (Figure 2d), indicating the successful replacement of EGFP with PSMA via the dual-plasmid platform.

Characterization of EGFP-eGVs and PSMA-eGVs

Transmission electron microscopy (TEM) analysis showed that both PSMA-eGVs and EGFP-eGVs had typical cylindrical structures with uniform morphology (Figure 3a and b). The structural integrity of PSMA-eGVs was further confirmed by cryo-EM analysis (Figure 3c). The results of particle size and potential characterization showed that the average particle size of PSMA-eGVs was 125.90 ± 4.70 nm (PDI = 0.057 ± 0.019), and the surface potential was −27.28 ± 2.56 mV. The average particle size of EGFP-eGVs was 126.22 ± 2.13 nm (PDI = 0.058 ± 0.024), and the surface potential was −29.88 ± 1.53 mV (Figure 3d–g). Morphometric analysis of 200 randomly selected GVs using ImageJ indicated that EGFP-eGVs measured 247.07 ± 53.46 nm in length and 91.16 ± 16.88 nm in width, whereas PSMA-eGVs displayed 242.78 ± 78.85 nm in length and 100.42 ± 18.25 nm in width (Figure 3h and i). Stability assessments over a 30-day period confirmed that the PSMA-eGVs maintained consistent size

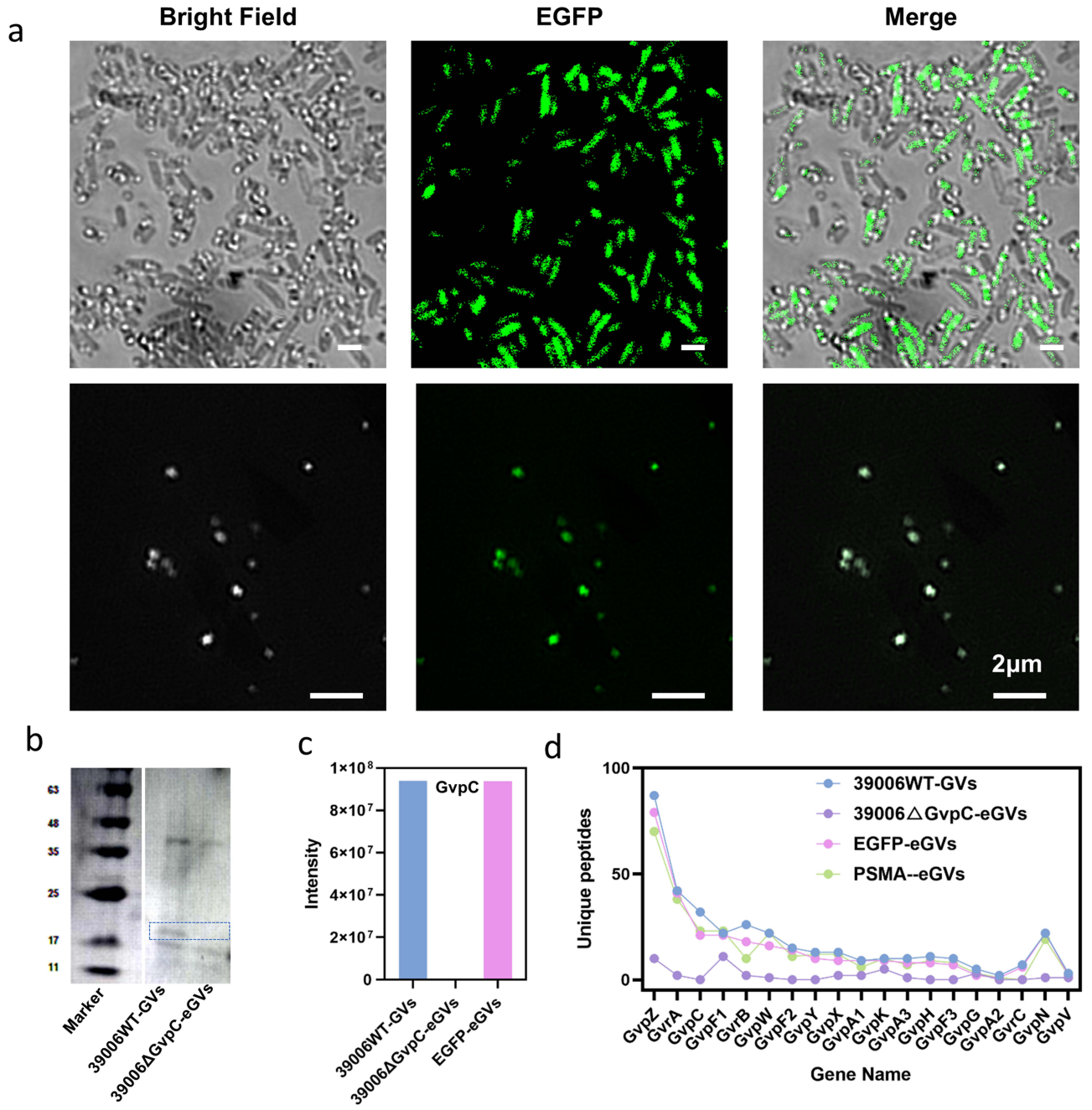

Figure 2 Characterization and protein validation of engineered Gas Vesicles (eGVs). (**a**) Bright-field, EGFP fluorescence, and merged images of EGFP-eGVs dual-plasmid bacteria and EGFP-eGVs vesicles. Scale bar: 2 μm. (**b**) SDS-PAGE results: 39006ΔGvpC-GVs lack the ~18 kDa GvpC protein band (blue dashed box). (**c** and **d**) Mass spectrometry proteomics analysis: GvpC peptides are completely absent in 39006ΔGvpC-eGVs; EGFP-eGVs exhibit GvpC abundance comparable to 39006WT-GVs; PSMA-eGVs display a protein profile consistent with EGFP-eGVs, indicating successful construction of targeted vesicles.

distribution and surface charge (Figure 3j and k). In vitro imaging performance evaluation showed that both PSMA-eGVs and EGFP-eGVs showed concentration-dependent signal enhancement, with comparable contrast signal intensities at the same concentration (Figure 3l and m). These results collectively validated the structural and functional reliability of the genetically engineered gas vesicles.

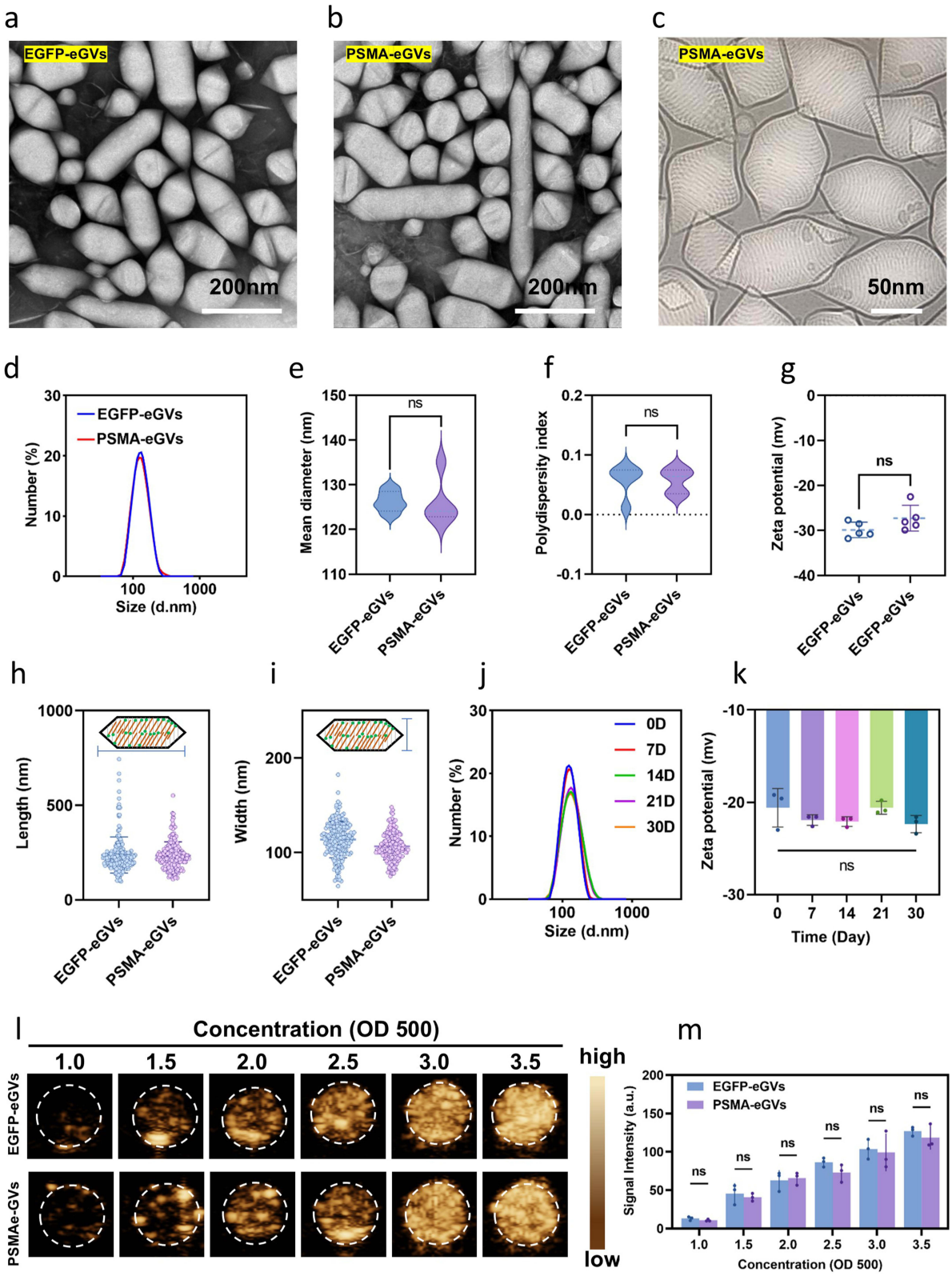

Figure 3 Characterization of EGFP-eGVs and PSMA-eGVs. (**a**) TEM images of EGFP-eGVs. (**b**) TEM images of PSMA-eGVs. (**c**) cryo-EM analysis of PSMA-eGVs. (**d**) Size distribution of EGFP-eGVs and PSMA-eGVs (n = 5). (**e**) The mean diameters of EGFP-eGVs and PSMA-eGVs (n = 5). (**f**) PDI of EGFP-eGVs and PSMA-eGVs. (**g**) Zeta potential of EGFP-eGVs and PSMA-eGVs (n = 5). (**h**) Average length of individual EGFP-eGVs and PSMA-eGVs (n = 200). (**i**) Average width of individual EGFP-eGVs and PSMA-eGVs (n = 200). (**j**) Particle size of PSMA-eGVs over 30-day period. (**k**) Zeta potential of PSMA-eGVs over 30-day period. (**l**) The representative ultrasound contrast images of EGFP-eGVs and PSMA-eGVs at different concentrations. (**m**) The quantitative analysis of EGFP-eGVs and PSMA-eGVs (n = 3). ns indicates no statistical difference.

https://doi.org/10.2147/IJN.S561230

In vitro Cell Targeting Studies

Molecular targeting is another key capability for molecular imaging agents. To systematically evaluate the targeting capability of this molecular probe, we conducted quantitative and qualitative verification of its specificity through in vitro flow cytometry analysis and cell adhesion assays. Flow cytometry analysis revealed that FITC-labeled PSMA-eGVs specifically bound to LNCap cells, whereas control EGFP-eGVs showed minimal binding activity. Notably, pre-blocking with an anti-PSMA polyclonal antibody significantly reduced the binding efficiency of FITC-PSMA-eGVs to LNCap cells, confirming their targeting specificity (Figure 4a, top row; S5). In PSMA-negative PC-3 cells, no significant binding was observed (Figure 4a, top row). Quantitative analysis indicated that 81% of LNCap cells treated

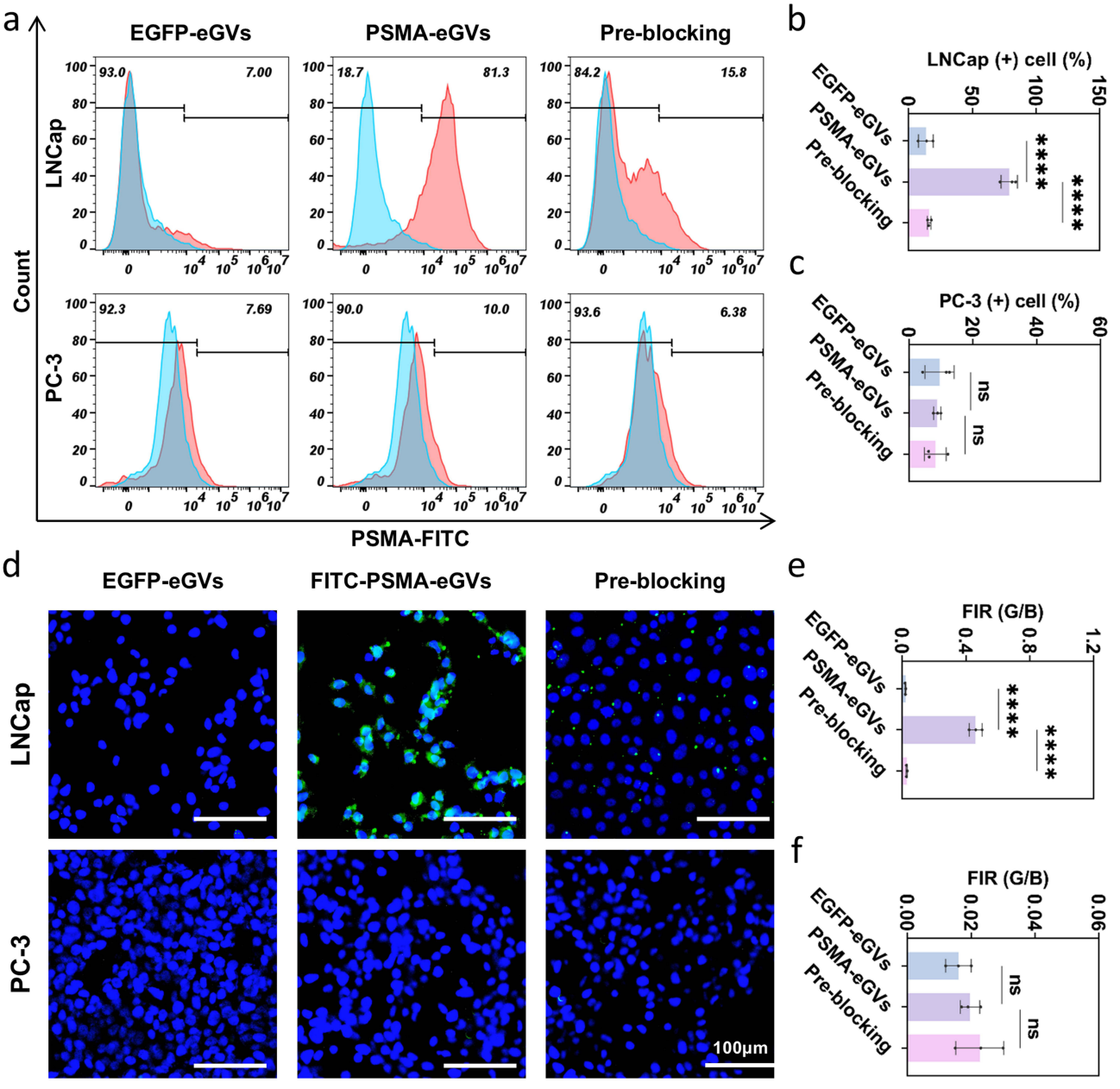

Figure 4 In vitro cell targeting studies. (**a**) Flow cytometry assay of LNCap cells and PC-3 cells incubated with EGFP-eGVs, FITC-PSMA-eGVs or anti-PSMA polyclonal antibodies + FITC-PSMA-eGVs, respectively. (**b**) Quantitative analysis of LNCap cells binding with EGFP-eGVs or FITC-PSMA-eGVs. (**c**) Quantitative analysis of PC-3 cells binding with EGFP-eGVs or FITC-PSMA-eGVs. (**d**) Representative fluorescent microscope images of PC-3 cells and LNCap cells incubated with EGFP-eGVs, FITC-PSMA-eGVs or anti-PSMA polyclonal antibodies + FITC-PSMA-eGVs, respectively. Green stands for FITC or EGFP, and blue for cell nuclei stained with DAPI. Scale bar: 100 μm. (**e**) and (**f**) Quantitative analysis of fluorescence intensities from(d). ns indicates no statistical difference, **** for $P < 0.0001$.

with FITC-PSMA-eGVs exhibited fluorescence enhancement compared to only 7% of cells treated with EGFP-eGVs (Figure 4b). In PC-3 cells, the rate of fluorescence enhancement was below 10% in both the groups (Figure 4c). In monolayer cell culture experiments, FITC-PSMA-eGVs demonstrated substantial binding to LNCap cells, whereas EGFP-eGVs showed negligible binding (Figure 4d, top row). Pre-incubation with the free anti-PSMA polyclonal antibody reduced vesicle-cell binding by more than 10-fold (Figure 4e). No effective binding occurred in PC-3 cells (Figure 4d, bottom row; 4f), further validating PSMA-mediated targeting specificity. These results collectively demonstrate that PSMA-eGVs possess specific recognition and efficient targeting capabilities toward PSMA-positive tumor cells.

In vivo Tumor Imaging Performance

We further evaluated the in vivo imaging performance of PSMA-eGVs in a tumor-bearing mouse model. This study employed two prostate cancer models, PSMA-high-expressing LNCap tumors and PSMA-negative PC-3 tumors, with subgroups stratified by tumor size (small: diameter <8 mm; large: diameter >10 mm). Pre-injection baseline imaging confirmed the absence of specific contrast signals in all tumor regions. Following systemic administration of gas vesicles, all groups exhibited rapid contrast enhancement, peaking within 10–30 s. In PSMA-negative PC-3 tumors, both small and large lesions showed rapid signal decay after injection of either PSMA-eGVs or EGFP-eGVs (Figure 5a, top row). Quantitative analysis revealed no statistically significant difference in the signal intensity between the two formulations (Figure 5b and c). Furthermore, the curve (AUC) analysis demonstrated no significant difference between small and large tumors in the PSMA-eGVs group (10,823 ± 2,094 a.u. vs 13,246 ± 3,066 a.u.; $p > 0.05$; Figure 5d), confirming the absence of specific targeting in PSMA-negative tumors. Conversely, PSMA-high-expressing LNCap tumors exhibited distinct behaviors. Although small tumors showed comparable initial peak signals (PSMA-eGVs: 52.9 ± 7.8 a.u. vs EGFP-eGVs: 38.5 ± 6.3 a.u.; $p > 0.05$), PSMA-eGVs demonstrated significantly prolonged signal retention (Figure 5a, bottom row). At 3 min post-injection, PSMA-eGVs maintained intensity at 40.2 ± 7.5 a.u., whereas EGFP-eGVs decayed to 9.3 ± 1.2 a.u. Dynamic imaging revealed substantially slower signal decay kinetics for PSMA-eGVs, generating 4.3-, 6.7-, and 8.5-fold higher intensities than EGFP-eGVs at 3-, 5-, and 10-minutes post-injection, respectively. This targeting imaging effect was consistently observed in large tumors (Figure 5e and f). AUC analysis showed no significant size-dependent differences (21,251 ± 3,934 a.u. vs 17,888 ± 350 a.u.; $p > 0.05$; Figure 5g), indicating the stable targeting efficacy of PSMA-eGVs across tumor volumes in PSMA-positive models.

In vivo PET-CT Imaging

Figure 6a showed the in vivo biodistribution of ^{18}F-PSMA in xenograft models of LNCap and PC-3 tumors. PET imaging 1.5 hours post-injection revealed no significant radiotracer uptake in PC-3 tumor-bearing mice, regardless of tumor volume (Figure 6a and b), whereas LNCap tumors exhibited substantial ^{18}F-PSMA accumulation. Quantitative analysis demonstrated significantly increased SUVmax values in the LNCap group, with large-volume tumors showing higher uptake than small tumors (2.66 ± 0.102 vs 3.14 ± 0.307; $p < 0.05$; Figure 6c). These findings indicate ^{18}F-PSMA possesses high specificity for PSMA-positive tumors and enhanced diagnostic sensitivity for larger lesions, visually validating its clinical utility as a prostate cancer-specific molecular probe.

Tumor Immunofluorescence Staining

Immunohistochemical (IHC) and hematoxylin-eosin (HE) staining analyses revealed distinct PSMA expression patterns in tumor, with positive immunoreactivity clearly detected in LNCap cells, but absent in PC-3 cells (Figure 6d and S6). Quantitative analysis demonstrated a significantly higher mean fluorescence intensity in large LNCap tumors than in the other groups (Figures 6e and f), consistent with our PET/CT imaging findings. Notably, the ultrasound molecular imaging approach employed in this study maintained consistent detection efficacy across tumors of varying sizes, demonstrating high sensitivity even in small tumor models. This capability provides a significant technical advantage for early detection of lesions.

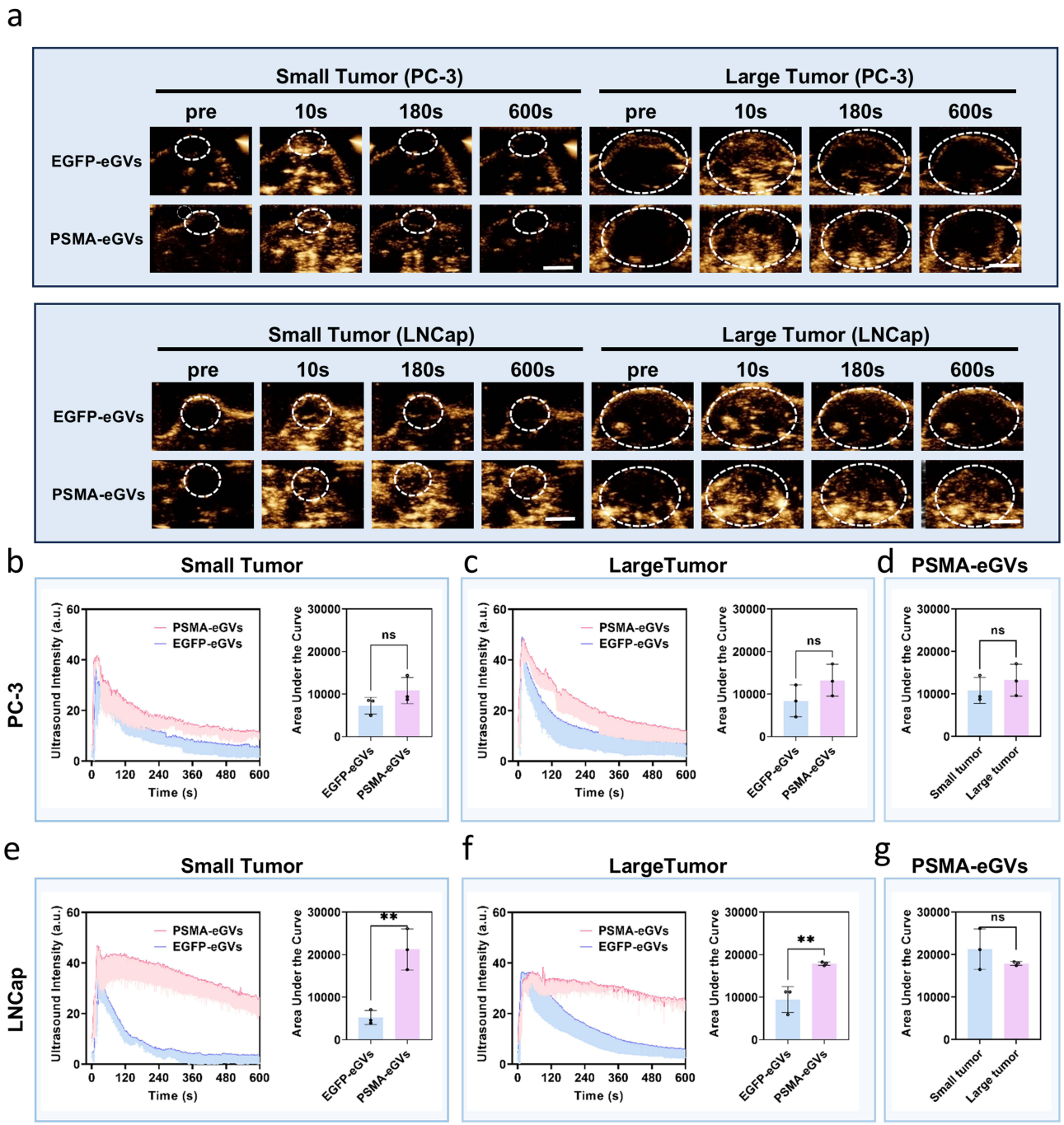

Figure 5 In vivo ultrasound molecular imaging (UMI) of prostate cancer xenograft models. (**a**) Representative UMI images of small and large tumors in mice bearing PC-3 (top row) or LNCap (bottom row) xenografts after intravenous injection of EGFP-eGVs or PSMA-eGVs. Time points: baseline (pre-injection), 10s, 180s, and 600s post-injection. (**b**) Time-intensity curves (TICs, left) and corresponding area under the curve (AUC, right) for small PC-3 tumors. (**c**) TICs (left) and AUC (right) for large PC-3 tumors. (**d**) AUC comparison between small and large PC-3 tumors injected with PSMA-eGVs. (**e**) TICs (left) and AUC (right) for small LNCap tumors. (**f**) TICs (left) and AUC (right) for large LNCap tumors. (**g**) AUC comparison between small and large LNCap tumors injected with PSMA-eGVs. Data represent mean ± SEM (n=3). ns indicates no statistical difference, **P < 0.01 indicates statistically significant differences.

Correlation of UMI and PET Metabolic Parameters with Immunohistochemical PSMA Staining

Subsequently, we correlated the ultrasound molecular imaging (UMI) area under the curve (AUC) with the PET/CT metabolic parameters and IHC staining. In PSMA-positive LNCap tumors, the UMI signal intensity showed a significant positive correlation with PET-CT SUVmax, yielding $R^2 = 0.90$ for small tumors (Figure 6g), and $R^2 = 0.94$ for large

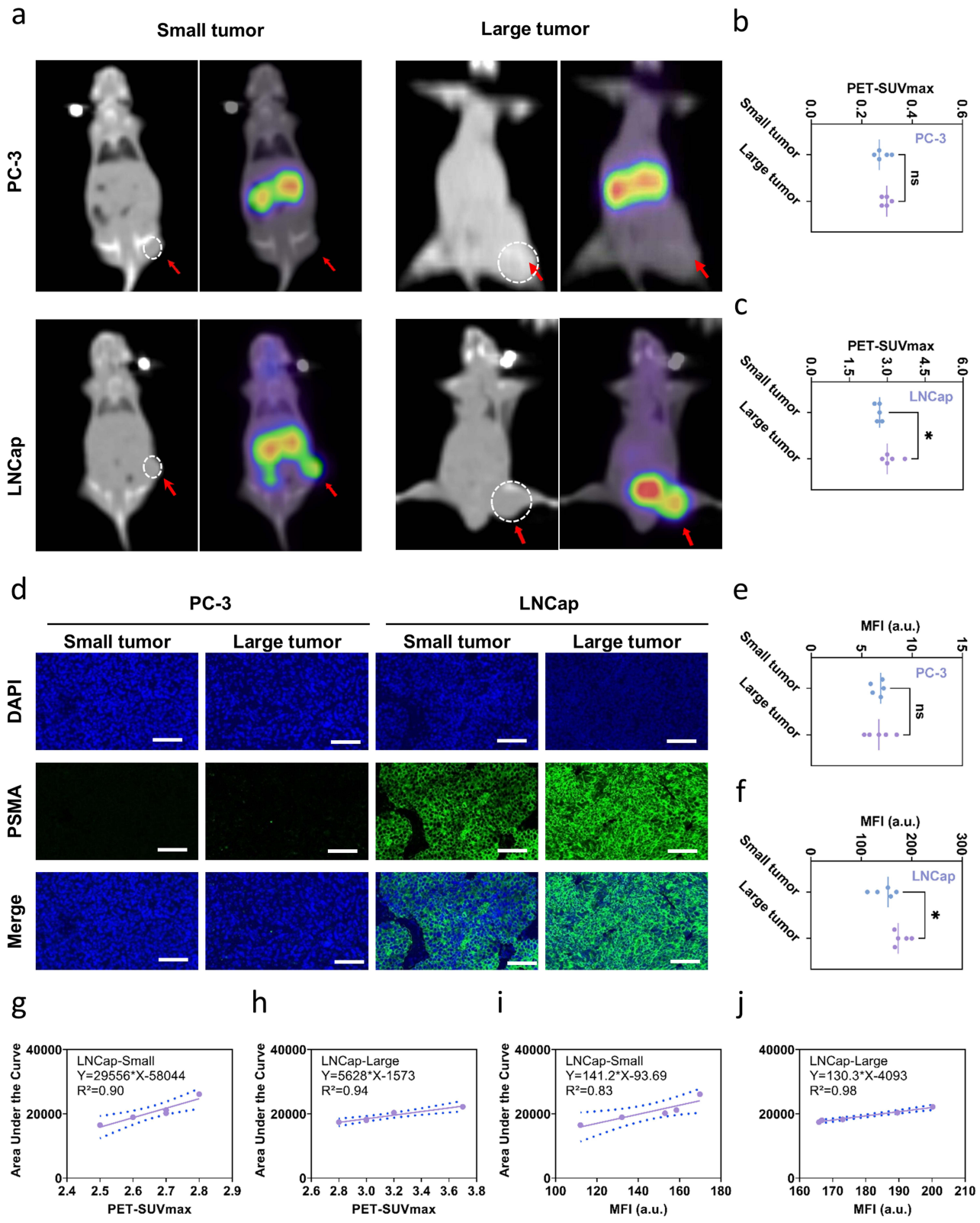

Figure 6 Comparative assessment of PET-CT metabolic activity, IHC, and UMI signals with quantitative correlation analysis. (**a**) Representative ^{18}F-PSMA PET/CT images of small and large tumors in LNCap and PC-3 models. Dashed circles outline tumor ROIs; left: CT; right: PET. (**b** and **c**) Quantitative comparison of ^{18}F-PSMA SUVmax in small and large tumors for PC-3 and LNCap xenografts. (**d**) Representative images of DAPI staining (blue, nuclei), PSMA IHC staining (green, PSMA expression), and merged images for small and large tumors derived from PC-3 and LNCap cells. Scale bar = 200 μm. (**e** and **f**) Comparison of mean fluorescence intensity (MFI) between small and large tumors derived from PC-3 and LNCap cells. MFI in large LNCap tumors was significantly higher than in small LNCap tumors. (**g–j**) Linear regression analyses correlating ^{18}F-PSMA PET/CT SUV values or PSMA expression levels with ultrasound molecular imaging AUC after PSMA-eGVs injection in small (**g, i**) and large (**h, j**) LNCap tumors. Data represent n = 5 animals per group. ns indicates no statistical difference, *P < 0.05 indicates statistically significant differences.

https://doi.org/10.2147/IJN.S561230

tumors (Figure 6h). Additionally, UMI signals demonstrated a strong correlation with PSMA expression levels quantified by IHC, with $R^2 = 0.83$ for small tumors and $R^2 = 0.98$ for large tumors (Figure 6i and j). These results demonstrated that the biosynthetic-targeted probes can accurately reflect tumor PSMA expression levels while maintaining comparable sensitivity to PET-CT for small lesion detection, supporting their clinical potential for early prostate cancer diagnosis.

Biosafety Assay

The hemolysis test results are shown in Figure S7a, revealing that there was no hemolysis or agglutination of erythrocytes at different concentrations of PSMA-eGVs. In contrast, hemolysis was observed in H_2O-treated samples as a positive control. In addition, the supernatants of the samples treated with PSMA-eGVs were transparent and colorless after centrifugation, similar to those of the PBS-treated sample. Further quantitative analysis showed that the hemolysis rate of PSMA-eGVs at different concentrations was all less than 5% (Figure S7b), suggesting that PSMA-eGVs did not damage red blood cells.

In addition, in vivo biosafety was analyzed using blood samples from healthy mice injected with PSMA-eGVs or EGFP-eGVs. The data revealed that the blood biochemical indices, such as liver and kidney function, showed no obvious abnormal changes (Figure S7c–g). HE staining analysis did not reveal pathological damage to the heart, liver, spleen, lungs, or kidneys, similar to PBS-treated controls (Figure S8). These results suggest that the PSMA-eGVs exhibit excellent biosafety.

Discussion

Prostate cancer is a common malignancy in elderly men, with severe health effects on their life.[27] Although transrectal ultrasonography has become a routine method for disease biopsy, monitoring, and efficacy evaluation, clinical studies have shown that its sensitivity and specificity still need to be improved.[28–30] Ultrasound molecular imaging, which integrates ultrasound imaging and molecular biology, provides a new method for early diagnosis of prostate cancer.[31,32] At present, the microbubbles-based probes such as BR55 mainly target molecules related to angiogenesis due to their relatively large particle size, resulting in their disability to bind with prostate cancer cells and specifically diagnosis of prostate cancer.[33,34] By contrast, nanobubbles-based probes exhibit significant advantages in the molecular imaging of the tumor cells due to their high permeability and retention effect in tumors.[35] Lots of literatures confirmed that nanobubbles could cross the vascular endothelial space of tumors.[14,36,37]

Unlike traditional synthesis of targeted nanobubble probes which needs multistep chemical coupling process,[38,39] we employed a genetically engineering strategy to synthesize targeted nanobubble probes in bacteria, the fabrication procedure and reducing the disordered ligand orientation and batch-to-batch variations. In this study, we used the temperature controlled gene expression strategy to induce the production of GvpC-PSMA fusion protein after synthesis of ΔGvpC-eGVs, which can decreasing the interference of anti-PSMA antibody protein and achieving precise self-assembly of PSMA-eGVs through the specific interaction of the GvpC domain.[40] Moreover, the probe preparation time can be shortened to 40 hours, significantly reducing the production costs. In addition, the strategy may allow us rapid shift from PSMA-eGVs to other ultrasound molecular imaging probes, only through simple replacement of the anti-PSMA antibody-coding gene sequence in pBV220 plasmid.

In this study, the resulting PSMA-eGVs exhibited good physical stability and targeting abilities. The mean particle size of PSMA-eGVs remained stable at approximately 120 nm over 30 days. In vitro experiments showed that the binding ability of PSMA-eGVs to prostate cancer cells was significantly higher than that of the non-targeted EGFP-eGVs. In vivo experiments in tumor-bearing mice confirmed that PSMA-eGVs produced a stronger and more persistent ultrasound signal in the tumor region than the control probe. These results suggest that PSMA-eGVs can selectively aggregate in tumor tissues and enhance tumor contrast signals. More importantly, in vivo ultrasound imaging signals of PSMA-eGVs in tumor-bearing mice showed good correlation with clinicopathological diagnosis and PET metabolism. Obviously, the current clinical diagnostic methods for prostate cancer, such as needle biopsy, are invasive. PSMA-PET, although non-invasive, is expensive and has radiation risks. By contrast, ultrasound molecular imaging technology with PSMA-eGVs has great advantages due to its non-invasiveness and low cost. Notably, the PSMA-eGVs probe possess good detection sensitivity in a small tumor, making it possible use in the early diagnosis of prostate cancer.

Nonetheless, this study still has some limitations. Firstly, the subcutaneous tumor model used in this study is different from the tumor which occurs in humans. An orthotopic prostate cancer model will be able to provide more convincing evidences. Secondly, there are approximately 15% of prostate cancer patients with low even lack of PSMA expression. In such cases, the development of multi-target probes may be necessary. Although the current work evaluated the in vivo biocompatibility through histopathological examination and serum biochemical analysis, and demonstrated good blood compatibility in vitro, the cytotoxicity, in vivo biodistribution, and genotoxicity of PSMA-eGVs still need to be comprehensively investigated for the future clinical translation application.

Conclusions

In conclusion, this study successfully established a one-step biosynthesis platform utilizing genetically engineered technology for the efficient production of targeted ultrasound molecular imaging probes. Using PSMA-positive prostate cancer as a model, we demonstrated that the biosynthesized PSMA-eGVs exhibit high targeting imaging performance of prostate cancer. Our study provides a promising strategy for developing targeted ultrasound probes for the non-invasive diagnosis of tumor.

Acknowledgments

The authors acknowledge the Core Facility of Shenzhen Institute of Synthetic Biology for providing access to the structured illumination super-resolution microscope (Nikon N-SIM) and extend appreciation to the engineers for their professional assistance in image acquisition.

Author Contributions

All authors made a significant contribution to the work reported, whether that is in the conception, study design, execution, acquisition of data, analysis and interpretation, or in all these areas; took part in drafting, revising or critically reviewing the article; gave final approval of the version to be published; have agreed on the journal to which the article has been submitted; and agree to be accountable for all aspects of the work.

Funding

This research is supported by the National Key R&D Program of China (2025YFA0922100), Shenzhen Medical Research Fund (grant no. D2301012, B2402006), the National Natural Science Foundation of China (32171365, 82572261), the Leading Talents of the Guangdong Special Support Program (2024TX08A098), Shenzhen High-level Hospital Construction Fund, the Shenzhen Natural Science Foundation General Program (JCYJ20250604180550063).

Disclosure

The authors declare that this research was conducted in the absence of any commercial or financial relationships that could be construed as potential conflicts of interest.

References

1. Lakes J, Arsov C. PSA screening and molecular markers. *Urologe A*. 2019;58(5):486–493. doi:10.1007/s00120-019-0900-y
2. Bakht MK, Beltran H. Biological determinants of PSMA expression, regulation and heterogeneity in prostate cancer. *Nat Rev Urol*. 2025;22(1):26–45. doi:10.1038/s41585-024-00900-z
3. Sekhoacha M, Riet K, Motloung P, Gumenku L, Adegoke A, Mashele S. Prostate Cancer Review: genetics, Diagnosis, Treatment Options, and Alternative Approaches. *Molecules*. 2022;27(17):5730. doi:10.3390/molecules27175730
4. Kohaar I, Petrovics G, Srivastava S. A Rich Array of Prostate Cancer Molecular Biomarkers: opportunities and Challenges. *Int J Mol Sci*. 2019;20(8):1813. doi:10.3390/ijms20081813
5. Kelloff GJ, Choyke P, Coffey DS. Challenges in clinical prostate cancer: role of imaging. *AJR Am J Roentgenol*. 2009;192(6):1455–1470. doi:10.2214/AJR.09.2579
6. Hao Y, Li Z, Luo J, Li L, Yan F. Ultrasound Molecular Imaging of Epithelial Mesenchymal Transition for Evaluating Tumor Metastatic Potential via Targeted Biosynthetic Gas Vesicles. *Small*. 2023;19(21):e2207940. doi:10.1002/smll.202207940
7. Liu T, Liang X, Liu W, et al. iRGD-Targeted Biosynthetic Nanobubbles for Ultrasound Molecular Imaging of Osteosarcoma. *Int J Nanomed*. 2025;20:791–805. doi:10.2147/IJN.S494151

8. Zhong J, Su M, Jiang Y, et al. VEGFR2 targeted microbubble-based ultrasound molecular imaging improving the diagnostic sensitivity of microinvasive cervical cancer. *J Nanobiotechnology*. 2023;21(1):220. doi:10.1186/s12951-023-01984-2
9. Wang Y, Fu M, Yang Y, et al. Modification of PEG reduces the immunogenicity of biosynthetic gas vesicles. *Front Bioeng Biotechnol*. 2023;11:1128268. doi:10.3389/fbioe.2023.1128268
10. Walsby AE. Gas vesicles. *Microbiol Rev*. 1994;58(1):94–144. doi:10.1128/mr.58.1.94-144.1994
11. Hill AM, Salmond GPC. Microbial gas vesicles as nanotechnology tools: exploiting intracellular organelles for translational utility in biotechnology, medicine and the environment. *Microbiology*. 2020;166(6):501–509. doi:10.1099/mic.0.000912
12. DasSarma S, DasSarma P. Gas Vesicle Nanoparticles for Antigen Display. *Vaccines (Basel)*. 2015;3(3):686–702. doi:10.3390/vaccines3030686
13. Shapiro MG, Goodwill PW, Neogy A, et al. Biogenic gas nanostructures as ultrasonic molecular reporters. *Nat Nanotechnol*. 2014;9(4):311–316. doi:10.1038/nnano.2014.32
14. Wei M, Lai M, Zhang J, Pei X, Yan F. Biosynthetic Gas Vesicles from Halobacteria NRC-1: a Potential Ultrasound Contrast Agent for Tumor Imaging. *Pharmaceutics*. 2022;14(6):1198. doi:10.3390/pharmaceutics14061198
15. Maresca D, Lakshmanan A, Lee-Gosselin A, et al. Nonlinear ultrasound imaging of nanoscale acoustic biomolecules. *Appl Phys Lett*. 2017;110 (7):073704. doi:10.1063/1.4976105
16. Englert C, Pfeifer F. Analysis of gas vesicle gene expression in Haloferax mediterranei reveals that GvpA and GvpC are both gas vesicle structural proteins. *J Biol Chem*. 1993;268(13):9329–9336. doi:10.1016/S0021-9258(18)98354-7
17. Pfeifer F. Distribution, formation and regulation of gas vesicles. *Nat Rev Microbiol*. 2012;10(10):705–715. doi:10.1038/nrmicro2834
18. DasSarma P, Karan R, Kim JM, Pecher W, DasSarma S. Bioengineering novel floating nanoparticles for protein and drug delivery. *Mater Today Proc*. 2016;3(2):206–210. doi:10.1016/j.matpr.2016.01.058
19. Hayes PK, Lazarus CM, Bees A, Walker JE, Walsby AE. The protein encoded by gvpC is a minor component of gas vesicles isolated from the cyanobacteria Anabaena flos-aquae and Microcystis sp. *Mol Microbiol*. 1988;2:545–552. doi:10.1111/j.1365-2958.1988.tb00062.x
20. Kim JM, Kim YS, Kim YR, Choi MJ, DasSarma P, DasSarma S. Bioengineering of Halobacterium sp. NRC-1 gas vesicle nanoparticles with GvpC fusion protein produced in E. coli. *Appl Microbiol Biotechnol*. 2022;106(5–6):2043–2052. doi:10.1007/s00253-022-11841-1
21. DasSarma S, Damerval T, Jones JG, Tandeau de Marsac N. A plasmid-encoded gas vesicle protein gene in a halophilic archaebacterium. *Mol Microbiol*. 1987;1(1):365–370. doi:10.1111/j.1365-2958.1987.tb01943.x
22. Tang S, Zhao C, Zhu X. Engineering Escherichia coli-Derived Nanoparticles for Vaccine Development. *Vaccines (Basel)*. 2024;12(11). doi:10.3390/vaccines12111287
23. Monson RE, Tashiro Y, Salmond GPC. Overproduction of individual gas vesicle proteins perturbs flotation, antibiotic production and cell division in the enterobacterium Serratia sp. ATCC 39006. *Microbiology*. 2016;162(9):1595–1607. doi:10.1099/mic.0.000347
24. Mimura Y, Katoh T, Saldova R, et al. Glycosylation engineering of therapeutic IgG antibodies: challenges for the safety, functionality and efficacy. *Protein Cell*. 2018;9(1):47–62. doi:10.1007/s13238-017-0433-3
25. Liu T, Wang J, Liu C, Wang Y, Li Z, Yan F. Characterization and Comparison of Contrast Imaging Properties of Naturally Isolated and Heterologously Expressed Gas Vesicles. *Pharmaceuticals*. 2024;17(6):755. doi:10.3390/ph17060755
26. Liu T, Wang J, Cui T, Yang L, Li Z, Yan F. Targeted Biosynthetic Nanobubbles for Ultrasound Molecular Imaging of Prostate Cancer. *Ultrasound Med Biol*. 2025;51(9):1447–1458. doi:10.1016/j.ultrasmedbio.2025.05.015
27. Sung H, Ferlay J, Siegel RL, et al. Global Cancer Statistics 2020: GLOBOCAN Estimates of Incidence and Mortality Worldwide for 36 Cancers in 185 Countries. *CA Cancer J Clin*. 2021;71(3):209–249. doi:10.3322/caac.21660
28. Ss T. Re: diagnostic Accuracy of Multi-Parametric MRI and TRUS Biopsy in Prostate Cancer (PROMIS): a Paired Validating Confirmatory Study. *J Urol*. 2017;198(1):101–102. doi:10.1016/j.juro.2017.04.055
29. Zamboglou C, Drendel V, Jilg CA, et al. Comparison of 68 Ga-HBED-CC PSMA-PET/CT and multiparametric MRI for gross tumour volume detection in patients with primary prostate cancer based on slice by slice comparison with histopathology. *Theranostics*. 2017;7(1):228–237. doi:10.7150/thno.16638
30. Merriel SWD, Pocock L, Gilbert E, et al. Systematic review and meta-analysis of the diagnostic accuracy of prostate-specific antigen (PSA) for the detection of prostate cancer in symptomatic patients. *BMC Med*. 2022;20(1):54. doi:10.1186/s12916-021-02230-y
31. Su C, Ren X, Nie F, et al. Current advances in ultrasound-combined nanobubbles for cancer-targeted therapy: a review of the current status and future perspectives. *RSC Adv*. 2021;11(21):12915–12928. doi:10.1039/D0RA08727K
32. Fan X, Wang L, Guo Y, et al. Ultrasonic Nanobubbles Carrying Anti-PSMA Nanobody: construction and Application in Prostate Cancer-Targeted Imaging. *PLoS One*. 2015;10(6):e0127419. doi:10.1371/journal.pone.0127419
33. Jain RK. Transport of molecules, particles, and cells in solid tumors. *Annu Rev Biomed Eng*. 1999;1(1):241–263. doi:10.1146/annurev.bioeng.1.1.241
34. Du J, Li XY, Hu H, Xu L, Yang SP, Li FH. Preparation and Imaging Investigation of Dual-targeted C(3)F(8)-filled PLGA Nanobubbles as a Novel Ultrasound Contrast Agent for Breast Cancer. *Sci Rep*. 2018;8(1):3887. doi:10.1038/s41598-018-21502-x
35. Shi Y, van der Meel R, Chen X, Lammers T. The EPR effect and beyond: strategies to improve tumor targeting and cancer nanomedicine treatment efficacy. *Theranostics*. 2020;10(17):7921–7924. doi:10.7150/thno.49577
36. Hao Y, Luo J, Wang Y, Li Z, Wang X, Yan F. Ultrasound molecular imaging of p32 protein translocation for evaluation of tumor metastasis. *Biomaterials*. 2023;293:121974. doi:10.1016/j.biomaterials.2022.121974
37. Matsumura Y, Maeda H. A new concept for macromolecular therapeutics in cancer chemotherapy: mechanism of tumoritropic accumulation of proteins and the antitumor agent smancs. *Cancer Res*. 1986;46(12 Pt 1):6387–6392.
38. Cheng Z, Al Zaki A, Hui JZ, Muzykantov VR, Tsourkas A. Multifunctional nanoparticles: cost versus benefit of adding targeting and imaging capabilities. *Science*. 2012;338(6109):903–910. doi:10.1126/science.1226338
39. Beck A, Goetsch L, Dumontet C, Corvaïa N. Strategies and challenges for the next generation of antibody-drug conjugates. *Nat Rev Drug Discov*. 2017;16(5):315–337. doi:10.1038/nrd.2016.268
40. Lakshmanan A, Farhadi A, Nety SP, et al. Molecular Engineering of Acoustic Protein Nanostructures. *ACS Nano*. 2016;10(8):7314–7322. doi:10.1021/acsnano.6b03364

International Journal of Nanomedicine

Dovepress
Taylor & Francis Group

Publish your work in this journal

The International Journal of Nanomedicine is an international, peer-reviewed journal focusing on the application of nanotechnology in diagnostics, therapeutics, and drug delivery systems throughout the biomedical field. This journal is indexed on PubMed Central, MedLine, CAS, SciSearch®, Current Contents®/Clinical Medicine, Journal Citation Reports/Science Edition, EMBase, Scopus and the Elsevier Bibliographic databases. The manuscript management system is completely online and includes a very quick and fair peer-review system, which is all easy to use. Visit http://www.dovepress.com/testimonials.php to read real quotes from published authors.

Submit your manuscript here: https://www.dovepress.com/international-journal-of-nanomedicine-journal